An Illustrative Model of Instabilities in Meridionally and Vertically Sheared Flows

NOBORU NAKAMURA

Program in Atmospheric and Oceanic Sciences, Princeton University, Princeton, New Jersey

(Manuscript received 16 September 1991, in final form 15 March 1992)

ABSTRACT

An analytic model is formulated to study the characteristics of shear instabilities in meridionally and vertically sheared flows. The model is based on the quasigeostrophic equations in two layers. The layers are divided into sections of piecewise uniform potential vorticity. An algebraic dispersion relation is obtained for the complex phase speed c. The magnitude and the sign of the potential vorticity jumps, their meridional separation, the barotropic shear, and the wavenumber of the modes determine the stability of the system. Solutions describe not only pure baroclinic and barotropic instabilities, but also mixtures of these instabilities. The influences of linearly sheared barotropic flows on baroclinic instability are studied in detail, with an emphasis on the direction of vertically integrated momentum flux. The model's implications for the nonlinear life cycle of baroclinic waves are also discussed.

1. Introduction

Our understanding of linear barotropic and baroclinic instabilities is based largely on models in which the basic state varies in only one dimension. That the atmospheric flow has meridional, vertical, and, to a lesser extent, zonal variations complicates the stability analysis. Eigenvalue problems linearized about the zonally averaged, climatological mean state are nonseparable in height and latitude and involve singularities at critical levels. To simplify the analysis, it is often assumed that the flow variation along the second dimension is small (Pedlosky 1964; McIntyre 1970; Held and Andrews 1983) or slow compared with the scale of the disturbance (i.e., the WKB approximation; Ioannou and Lindzen 1986). Unfortunately, these assumptions are hard to justify from observation. For example, the meridional scale of baroclinic eddies is often comparable to that of the westerly jet in which they are embedded (Stone 1969). Numerical techniques for two-dimensional eigenvalue problems (Moore and Peltier 1987; Lin and Pierrehumbert 1988), on the other hand, are often expensive and impractical for covering a wide range of parameter space. Consequently, few useful models have been available to date for elucidating the general stability of two-dimensional flows.

In this paper, we present a linear analysis of a highly simplified mathematical model of meridionally *and* vertically varying flows to illustrate the behavior of instabilities in such environments. For this purpose, the flow is divided into sections of uniform but distinct quasigeostrophic pseudo-potential vorticity (PV) and the solutions are matched across the PV discontinuities. The model, formulated in the next section, not only allows analytic solutions for pure baroclinic and barotropic instabilities (section 3), but also applies to more general cases where the instabilities grow under meridional and vertical shears. To demonstrate the model's versatility, the stability of baroclinic waves is analyzed for the case where a constant barotropic shear (section 4) and a linearly sheared jet (section 5) are added to the basic state. The changes in the growth rates and modal structure due to the barotropic shear are examined, with special emphasis on the direction of the vertically integrated momentum flux. The model's implications for the nonlinear life cycle of baroclinic waves are also discussed by comparing the analysis with independent nonlinear life-cycle simulations of baroclinic waves.

2. The model

The remarkable success of Eady's model (1949) and Phillips' two-layer model (1954) of baroclinic instability suggests that a limited number of discrete modes (two in these models) are enough to describe the rudimentary nature of shear instability. While two discrete vertical modes (edge waves) lead to baroclinic instability, two meridional modes resonate to produce barotropic instability under certain conditions.[1] When

Corresponding author address: Dr. Noboru Nakamura, Dept. of Geophysical Sciences, University of Chicago, 5734 S. Ellis Ave., Chicago, IL 60637.

[1] The "resonance" of modes as an instability mechanism is not restricted to the rotational (Rossby) modes, but also applies to divergent (gravity) modes, which gives rise to, for example, Kelvin–Helmholtz instability. For a recent development in the theory, see Hayashi and Young (1987) and Sakai (1989).

the zonal-mean flow varies in two dimensions, instabilities are likely to arise from meridional and vertical interactions among modes. Hence in the model described below, we retain two vertically discrete modes as well as two meridionally discrete modes, for a total of four, to allow such nonseparable interaction. (In section 5, the number of meridional modes will be increased to three.) We shall see that in addition to the pure baroclinic and barotropic instabilities, the model is capable of describing more general classes of instability.

A horizontally infinite, quasigeostrophic two-layer model with equal layer depths $H/2$ is divided into three regions in the meridional direction (Fig. 1). The quasigeostrophic pseudo-potential vorticity of the basic state is assumed to be uniform within each section, defined by a layer and a region, but can be discontinuous across the two vertical interfaces at $y = \pm L/2$ (and across the layer interface, which does not affect the quasigeostrophic dynamics since the vertical advection of the PV is neglected). Such discontinuity can be formed by discontinuous gradients in the zonal wind, as shall be illustrated later. The dynamics of the system is governed by the four PV discontinuities that generate four independent modes. When the PV jumps or delta-function meridional "gradients" include both signs, the flow can be unstable according to the Rayleigh–Kuo theorem (Fig. 1a), the Charney–Stern theorem (Fig. 1b), or both (Fig. 1c).

The basic-state PV, Q, has no meridional gradient within each section due to uniformity. Hence, assuming the f-plane approximation,

$$\frac{dQ_1}{dy} = -\frac{d^2U_1}{dy^2} + \frac{1}{L_R^2}(U_1 - U_2) \equiv 0 \quad (2.1a)$$

$$\frac{dQ_2}{dy} = -\frac{d^2U_2}{dy^2} - \frac{1}{L_R^2}(U_1 - U_2) \equiv 0, \quad (2.1b)$$

where subscripts 1 and 2 denote quantities in the upper and lower layers, respectively; $U_n(y)$ is the zonal velocity, and L_R is the internal Rossby radius of deformation. The notation is standard (e.g., Pedlosky 1987) unless otherwise stated.

If we introduce barotropic and baroclinic components of U as

$$U_B \equiv \frac{U_1 + U_2}{2}; \quad U_C \equiv \frac{U_1 - U_2}{2}, \quad (2.2)$$

then, from (2.1a) and (2.1b),

$$U_B(y) = ay + b;$$

$$U_C(y) = \alpha \exp(y/L_C) + \beta \exp(-y/L_C), \quad (2.3)$$

where a, b, α, β are constants and $L_C \equiv L_R/\sqrt{2}$. Thus, the uniform PV in the two-layer model requires that the barotropic component of the flow be linear and the baroclinic component (thermal wind) be exponential in y. Restrictive as it may seem, (2.3) turns out to be quite adequate for the illustrative purpose of the present study. The shape of the mean flow will be given in the subsequent sections.

Superposed on the mean flow is a normal-mode perturbation of the form

$$\psi_n(x, y, t) \equiv \hat{\psi}_n(y) \exp\{ik(x - ct)\}; \quad n = 1, 2. \quad (2.4)$$

The uniform basic-state PV allows a perturbation whose PV is exactly zero in each section:

$$\frac{\partial^2\psi_1}{\partial x^2} + \frac{\partial^2\psi_1}{\partial y^2} - \frac{1}{L_R^2}(\psi_1 - \psi_2) = 0 \quad (2.5a)$$

$$\frac{\partial^2\psi_2}{\partial x^2} + \frac{\partial^2\psi_2}{\partial y^2} + \frac{1}{L_R^2}(\psi_1 - \psi_2) = 0, \quad (2.5b)$$

where ψ is the perturbation streamfunction. Substituting (2.4) in (2.5), and defining the barotropic and baroclinic components as

$$\hat{\psi}_B \equiv \frac{\hat{\psi}_1 + \hat{\psi}_2}{2}; \quad \hat{\psi}_C \equiv \frac{\hat{\psi}_1 - \hat{\psi}_2}{2}, \quad (2.6)$$

one can rearrange (2.5) as

$$\hat{\psi}_B(y) = A \exp(-ky) + C \exp(ky) \quad (2.7a)$$

$$\hat{\psi}_C(y) = B \exp(-Ky) + D \exp(Ky), \quad (2.7b)$$

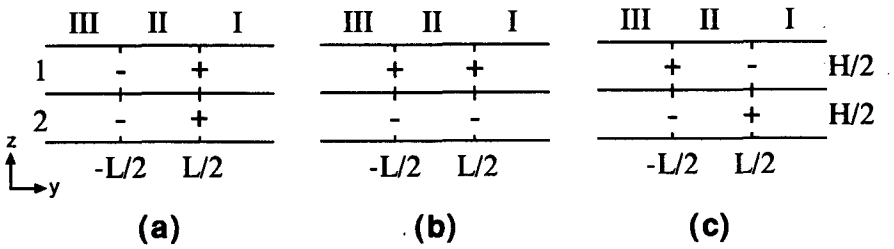

FIG. 1. Design of piecewise uniform PV model in two layers. The meridional PV discontinuities are indicated by their signs. (a) $Q_1^{III} > Q_1^{II} < Q_1^{I}$, $Q_2^{III} > Q_2^{II} < Q_2^{I}$, (b) $Q_1^{III} < Q_1^{II} < Q_1^{I}$, $Q_2^{III} > Q_2^{II} > Q_2^{I}$, (c) $Q_1^{III} < Q_1^{II} > Q_1^{I}$, $Q_2^{III} > Q_2^{II} < Q_2^{I}$, where Q is the basic-state PV.

where

$$K^2 \equiv k^2 + L_C^{-2}, \tag{2.8}$$

and A, B, C, and D are the complex constants that are to be determined simultaneously with the complex phase speed c.

We require that the amplitude of the modes vanish at $y = \pm\infty$. Hence,

$$A = B = 0 \quad y \leqslant -L/2 \tag{2.9a}$$

$$C = D = 0 \quad y \geqslant L/2. \tag{2.9b}$$

To be consistent with (2.9), the baroclinic wind U_C must also vanish at $y = \pm\infty$:

$$\lim_{y \to \pm\infty} U_C(y) = 0. \tag{2.10}$$

The matching conditions at the interfaces require the continuity in the meridional winds (both geostrophic and ageostrophic parts). For this to be satisfied, it is required that

$$\left.\begin{matrix} \hat{\psi}_n(y) \\ (U_n - c)\dfrac{d\hat{\psi}_n}{dy} + \left(f - \dfrac{dU_n}{dy}\right)\hat{\psi}_n \end{matrix}\right\} \text{ be continuous across}$$

$$y = \pm L/2 \quad (n = 1, 2). \tag{2.11}$$

The second condition in (2.11), which enforces the continuity in the ageostrophic meridional wind and brings about the time independence to the problem, is obtained by collecting terms in the momentum equation to the first order in the Rossby number. Alternatively, it can be obtained by integrating the quasigeostrophic PV equation across the discontinuity. Both $(U_n - c)$ and $\hat{\psi}_n$ are continuous across $y = \pm L/2$ but $f - dU_n/dy$ and $d\hat{\psi}_n/dy$ are not. It is convenient to rewrite (2.11) in terms of barotropic and baroclinic components defined in (2.6):

$$\hat{\psi}_B(y), \quad \hat{\psi}_C(y) \quad \text{continuous across} \quad y = \pm L/2, \tag{2.12a}$$

$$\left.\begin{matrix} (U_B - c)\dfrac{d\hat{\psi}_B}{dy} + \left(f - \dfrac{dU_B}{dy}\right)\hat{\psi}_B + U_C\dfrac{d\hat{\psi}_C}{dy} - \dfrac{dU_C}{dy}\hat{\psi}_C \\ U_C\dfrac{d\hat{\psi}_B}{dy} - \dfrac{dU_C}{dy}\hat{\psi}_B + (U_B - c)\dfrac{d\hat{\psi}_C}{dy} + \left(f - \dfrac{dU_B}{dy}\right)\hat{\psi}_C \end{matrix}\right\} \text{ continuous across } y = \pm L/2. \tag{2.12b}$$

The equations (2.7a, b) and the boundary conditions (2.9) (2.12) constitute an eigenvalue problem. The 13 unknowns, that is, four coefficients in (2.7) for three regions plus the complex phase speed c, shall be determined by the 12 independent boundary conditions (2.9) and (2.12), except for the arbitrariness in the amplitude of the mode. Due to the four time-dependent matching conditions (2.12b), the resultant dispersion relation will be generally quartic in c.

Once the eigenvalues and the meridional structure of the streamfunctions are obtained, the profiles of meridional heat and momentum fluxes can be computed. The heat flux is

$$\overline{\frac{\partial\psi_2}{\partial x}(\psi_1 - \psi_2)} = 2\left\{\overline{\frac{\partial\psi_B}{\partial x}\psi_C}\right\}$$

$$= (C_rD_i - C_iD_r)k\exp\{(k+K)y\} + (A_rD_i - A_iD_r)k\exp\{(K-k)y\} + (C_rB_i - C_iB_r)k\exp\{-(K-k)y\} + (A_rB_i - A_iB_r)k \times \exp\{-(k+K)y\}, \tag{2.13}$$

where the overbar denotes zonal averaging, and the subscripts r and i denote the real and imaginary parts of the complex coefficients, respectively. To give the dimension of heat flux, multiply (2.13) by $(f_0\theta_0)/(gH)$, where θ_0 is the mean potential temperature. If the mode consists of either barotropic or baroclinic component alone, so that $A = C = 0$ or $B = D = 0$, no vertical tilt appears in the modal structure and the heat flux vanishes identically. The vertically integrated momentum flux is

$$-\overline{\frac{\partial\psi_1}{\partial x}\frac{\partial\psi_1}{\partial y}} - \overline{\frac{\partial\psi_2}{\partial x}\frac{\partial\psi_2}{\partial y}} = -2\left(\overline{\frac{\partial\psi_B}{\partial x}\frac{\partial\psi_B}{\partial y}} + \overline{\frac{\partial\psi_C}{\partial x}\frac{\partial\psi_C}{\partial y}}\right)$$

$$= 2k\{k(C_rA_i - C_iA_r) + K(D_rB_i - D_iB_r)\}. \tag{2.14}$$

If the meridional structure of the mode is symmetric or antisymmetric within a region, or $(A, B) = \pm(C, D)$, the momentum flux vanishes identically. (There is no coherent meridional tilt.) Note also that the momentum flux does not depend on y within a region, and is identically zero in the two semi-infinite regions by virtue of (2.9). Both heat and momentum fluxes

vanish when the mode is neutral, so A, B, C, and D are all real.

The discontinuities in the momentum flux and in the PV across an interface ($y = y_0$) are related by

$$(\overline{uv})_n|^{y+} - (\overline{uv})_n|^{y-} = \frac{d_n\overline{\eta_n^2}}{dt}\Big|^{y_0}(Q_n|^{y+} - Q_n|^{y-})$$

$$\equiv \frac{2kc_i|\hat{\psi}_n|^2}{|U_n - c|^2}\Big|^{y_0}(Q_n|^{y+} - Q_n|^{y-}), \quad n = 1, 2, \quad (2.15)$$

where η is the meridional displacement of the interface and $d_n/dt \equiv \partial/\partial t + U_n\partial/\partial x$. The jump in the vertically integrated momentum flux is simply the sum of (2.15) over the two layers. It follows that if the PV discontinuity at an interface does not change sign between the two layers, the net momentum flux jump has the same sign as the PV discontinuity as long as the mode is growing. If, on the other hand, the PV discontinuity has opposite sign in the two layers, the discontinuity in the vertically integrated momentum flux can take either sign depending on the vertical structure of the mode (Held 1975).

3. Barotropic and baroclinic instabilities

Now consider a basic flow given by

$$\left.\begin{aligned} U_B(y) &= b(y - L/2) + aL/2 \\ U_C(y) &= U_0\cosh(L/2L_C) \\ &\quad \times \exp\{-(y - L/2)/L_C\}\end{aligned}\right\} \quad L/2 < y$$

$$\left.\begin{aligned} U_B(y) &= ay \\ U_C(y) &= U_0\cosh(y/L_C)\end{aligned}\right\} \quad -L/2 \leq y \leq L/2 \quad (3.1)$$

$$\left.\begin{aligned} U_B(y) &= b(y + L/2) - aL/2 \\ U_C(y) &= U_0\cosh(L/2L_C) \\ &\quad \times \exp\{(y + L/2)/L_C\}\end{aligned}\right\} \quad y < -L/2,$$

which satisfies (2.3) and (2.10). The geometry of this flow is sketched in Fig. 2. The sign and magnitude of the PV discontinuities at $y = \pm L/2$ are determined by the discontinuities in the vorticity associated with the barotropic and baroclinic components of the flow, namely

$$\delta \equiv a - b \quad \text{and} \quad \epsilon \equiv (U_0/L_C)\exp(L/2L_C). \quad (3.2)$$

The PV discontinuities associated with the barotropic component at $y = \pm L/2$ have equal strength but opposite sign, $\pm\delta$, satisfying the usual necessary condition for barotropic instability. The PV discontinuities in the baroclinic component are equal at $y = \pm L/2$ in each layer, but have opposite sign in the two layers, satisfying the necessary condition for baroclinic instability. The polarity of the four PV discontinuities corresponds to Fig. 1a when $\delta > \epsilon > 0$, and to Fig. 1b when $\epsilon > \delta > 0$.[2] The flow is uniquely determined when a, δ, ϵ, and L are given.

A perturbation streamfunction is sought in the form of (2.7) in each region. Using (2.9) and (2.12), one obtains four simultaneous equations for the four coefficients for the inner region ($-L/2 < y < L/2$)

$$\begin{pmatrix} pc + q & s & R & T \\ -s & pc - q & T & R \\ r & t & Pc + Q & S \\ t & r & -S & Pc - Q \end{pmatrix} \times \begin{pmatrix} C\exp(kL/2) \\ A\exp(kL/2) \\ D\exp(KL/2) \\ B\exp(KL/2) \end{pmatrix} = 0, \quad (3.3)$$

and a dispersion relation

$$c^4 - (w^+w^- + W^+W^- + z^+Z^+ + z^-Z^-)c^2 + (z^+Z^- - w^+W^-)(z^-Z^+ - w^-W^+) = 0, \quad (3.4)$$

where c is the complex phase speed. For the expression of parameters appearing in (3.3) and (3.4), refer to appendix A. Notice (3.4) is the result of vanishing determinant of the coefficient matrix in (3.3). Since (3.4) is quadratic in c^2, it can be solved analytically. The problem can be uniquely solved given the four flow parameters, δ, a, L, ϵ, and the wavenumber k. We start our analysis with some special cases characterized by a subset of these parameters to elucidate the basic dynamics included in the system.

a. No baroclinic flow

In the absence of baroclinic component of the flow or $U_0 \equiv 0$, it follows from appendix A that $\epsilon = z^+ = z^- = Z^+ = Z^- = 0$, and thus (3.4) simplifies to

$$(c^2 - w^+w^-)(c^2 - W^+W^-) = 0. \quad (3.5)$$

Vanishing of the first factor in the lhs yields a pair of barotropic modes (whose structure in the upper layer is identical with that in the lower layer), and the second factor corresponds to the internal or equivalent barotropic modes (the upper- and lower-layer structures are antiphase). The barotropic modes are identical with those found in the single-layer system (e.g., Garner et al. 1992), while the stratification is crucial to the internal modes. Since the two types of modes are decoupled, there is no vertical tilt in the modal structure; therefore, instability, if any, must be sustained barotropically. The barotropic modes yield a growing/damping pair when $w^+w^- < 0$, while the internal

[2] This flow does not support the PV configuration like Fig. 1c. For flows corresponding to Fig. 1c, jumps in $\partial U_C/\partial y$ must have opposite sign at $y = \pm L/2$.

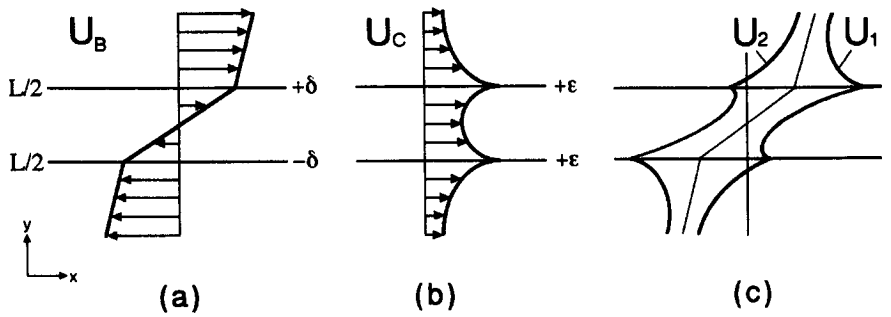

FIG. 2. Typical unstable flow profile of the model. (a) Barotropic component of the flow. (b) Baroclinic component of the flow. (c) Upper- and lower-layer flows. The associated PV jumps at the kinks are labeled. Note $U_1 = U_B + U_C$, $U_2 = U_B - U_C$.

modes become unstable when $W^+W^- < 0$. It is easy to show that these inequalities are realized only when $\delta a \equiv (a - b)a > 0$, which is a paraphrase of Fjørtoft's (1950) theorem.

Figure 3 shows the growth rates of barotropic and internal modes as a function of nondimensional wavenumber kL_R and the meridional separation of the PV discontinuities L/L_R, for the case of zero barotropic shear outside $y = \pm L/2$ ($b = 0$ or $\delta = a$). The growth rates are normalized by δ. This isolated shear layer appears widely in the literature (Rayleigh 1880; Eady 1949; Gill 1982, §13.6). For cases with nonzero b, see Garner et al. (1992). The barotropic modes are unstable over a wide range of wavenumber spectrum when the meridional separation is small, but unstable only at large scales when the meridional separation is large. The internal modes, on the other hand, are stable at all wavenumbers beyond certain meridional separation. The normalized growth rates of the barotropic modes are a function of kL only. The shortwave cutoff and maximum growth occur at

$$(kL)_c \equiv 1.2784 \quad \text{and} \quad (kL)_m \equiv 0.7968, \tag{3.6}$$

respectively. Similarly, the cutoff wavelengths for the internal modes are given by

$$(KL)_c \equiv 1.2784, \tag{3.7}$$

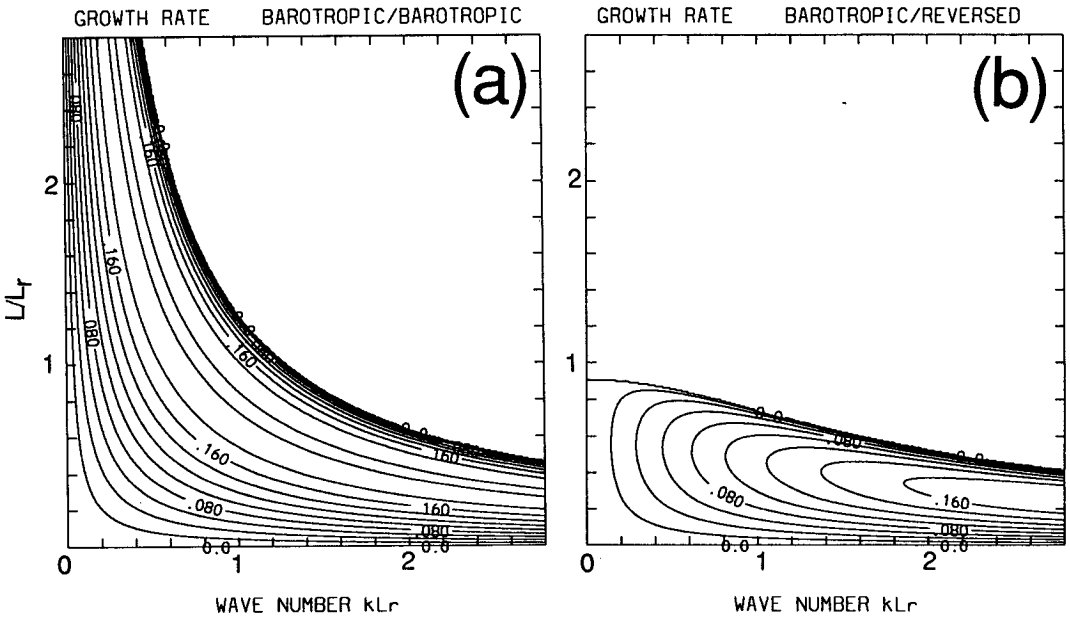

FIG. 3. Growth rate of barotropic instability with zero vorticity in the outer regions, as a function of zonal wavenumber and meridional separation. Both scales are normalized by the internal Rossby radius L_R, and the growth rate is normalized by the inner barotropic shear a. (a) Barotropic mode. (b) Internal (or equivalent barotropic) mode.

but their growth rates depend also on k/K. Since the minimum possible value for K is L_C^{-1} at $k = 0$ [(2.8)], the internal modes are stable for all wavenumbers when

$$L > 1.2784 L_C = 0.9040 L_R. \quad (3.8)$$

The meridional penetration scale for the internal modes (which consists only of the baroclinic component ψ_C) is K^{-1} [(2.7)], thus limited to an internal Rossby radius from the PV discontinuity. Since the penetration radius of the unstable modes must be comparable to the distance between the PV discontinuities, the internal modes cannot be unstable if the separation of the discontinuities exceeds the Rossby radius. The penetration scale for the barotropic modes, on the other hand, is k^{-1}, which allows the modes to adjust the wavelength to maintain instability for all values of L. The growth rates of the internal modes are generally smaller than those of the barotropic modes for the same wavenumber and flow parameters, but they converge in the shortwave limit.

b. *No barotropic flow*

When there is no barotropic flow ($a = b \equiv 0$), it follows $a = \delta = w^+ = w^- = W^+ = W^- = 0$, simplifying (3.4) to

$$(c^2 - z^+Z^+)(c^2 - z^-Z^-) = 0. \quad (3.9)$$

Vanishing of the first factor in the lhs represents a pair of modes with symmetric meridional structure about $y = 0$ (in streamfunction), whereas the second factor corresponds to the modes with antisymmetric structure. Antisymmetric modes disappear as L vanishes. This "single-interface" limit is analogous to the Heton cloud model studied by Pedlosky (1985). The symmetric modes develop a growing/damping pair when $z^+Z^+ < 0$, while the antisymmetric modes become unstable when $z^-Z^- < 0$. The shortwave cutoff of the symmetric modes can be easily derived as

$$k_C = L_C^{-1}. \quad (3.10)$$

This cutoff wavenumber is identical with that for the baroclinic waves in the conventional two-layer model on an f plane (Phillips 1954; Pedlosky 1987).

Figure 4 displays the growth rates of the symmetric and antisymmetric baroclinic modes as a function of nondimensional wavenumber and meridional separation. The symmetric modes are unstable over the entire longwave range $k < L_C^{-1}$. The growth rates slowly decrease with increasing meridional separation, though the zonal scale of the most unstable wave is unchanged. The antisymmetric modes, in contrast, are unstable only at large meridional separation. By requiring that the shortwave cutoff wavenumber be positive, the range of meridional separation in which antisymmetric modes are unstable is obtained as

$$L > 1.2784 L_C = 0.9040 L_R. \quad (3.11)$$

This threshold value coincides with the critical meridional separation for the internal modes of barotropic

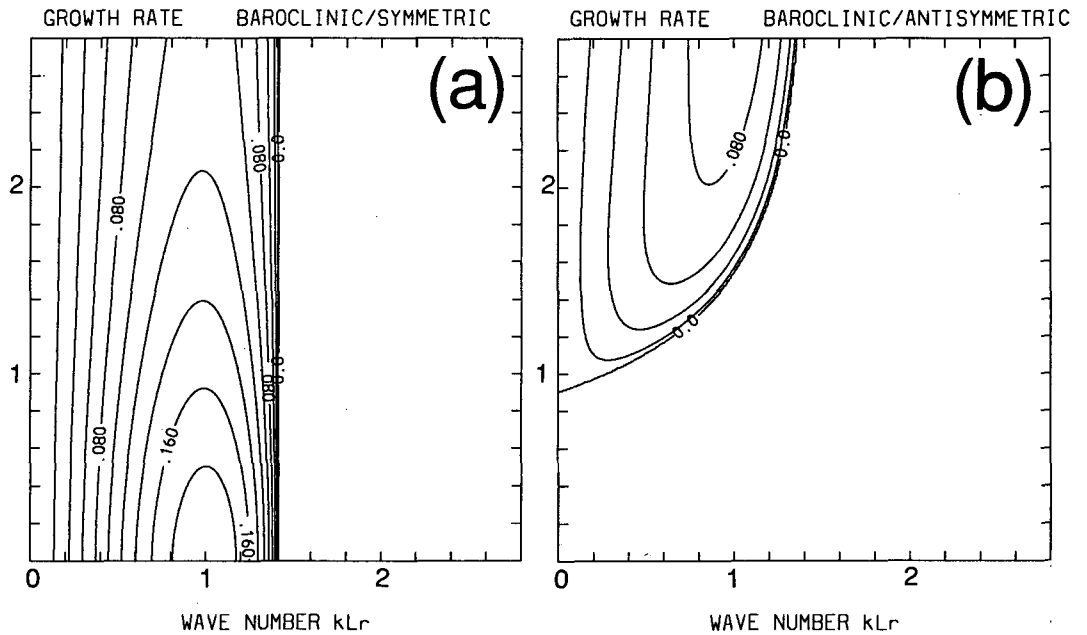

FIG. 4. Same as Fig. 3 but for baroclinic instability. The growth rate is normalized by the meridional PV jump ϵ. (a) Symmetric mode. (b) Antisymmetric mode.

instability [(3.8)]. The growth rates of antisymmetric modes are smaller than those of the symmetric modes for the same flow parameters, except at very small wavenumbers where the antisymmetric modes grow marginally faster. The growth rates of the two modes converge as L becomes large. Due to the meridional symmetry, neither mode sustains a net momentum flux.

4. Baroclinic instability with constant barotropic shear

In the preceding section we have seen that the model solutions include pure barotropic and baroclinic instabilities as special cases. If all the flow parameters in (3.4) are retained, however, one can solve more general cases where the flows vary meridionally *and* vertically. In such instances, the separation of modes illustrated before no longer holds and instability, if any, is likely to bear mixed characteristics of barotropic and baroclinic instabilities. To solve the most general case is beyond the scope of this paper. Instead, we focus our attention to a more specific question to which the model is conveniently applied: How is baroclinic instability modified under a barotropically sheared flow? The most recent and comprehensive study on this subject is that by James (1987), who numerically determines the stability of baroclinic waves that grow in meridionally sheared flows. He finds that horizontal shear in the flow suppresses the growth of baroclinic waves by limiting their meridional scale. In the following, we demonstrate that our analytic model reproduces the essence of James's numerical solution.

Assume that the barotropic flow in (3.1) is a Couette flow

$$U_B(y) = ay \quad -\infty < y < \infty, \tag{4.1}$$

so that $\delta \equiv a - b = 0$, while the baroclinic flow $U_C(y)$ in (3.1) remains the same. In this case, the barotropic flow by itself does not contribute to the PV discontinuities at the interfaces and hence, does not lead to instability. It does, however, modify the nature of baroclinic instability through the meridional shear a. The dispersion relation (3.4) becomes

$$c^4 - \left(\frac{a^2L^2}{2} + z^+Z^+ + z^-Z^-\right)c^2 + \left(z^+Z^- - \frac{a^2L^2}{4}\right)\left(z^-Z^+ - \frac{a^2L^2}{4}\right) = 0. \tag{4.2}$$

Notice that the barotropic shear is coupled with L; thus, the meridional separation is crucial in the effectiveness of the barotropic shear. In the absence of barotropic shear, (4.2) reduces to (3.9), recovering the symmetric and antisymmetric modes of baroclinic waves.

Figure 5 shows the growth rates of the baroclinic instability, derived from (4.2) and normalized by the baroclinic PV discontinuity ϵ, as a function of nondimensional wavenumber kL_R and barotropic shear a/ϵ for various meridional separations. The largest

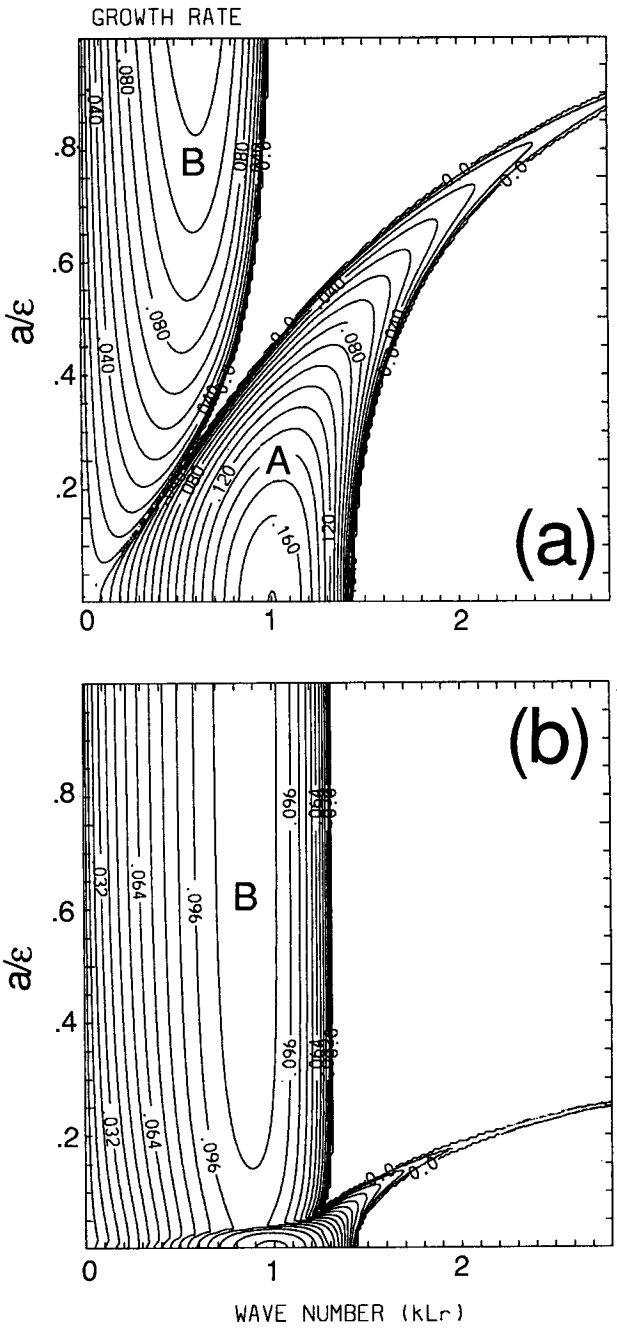

FIG. 5. Growth rate of baroclinic instability with constant barotropic shear as a function of wavenumber and barotropic shear. The wavenumber is normalized by the Rossby radius L_R, and the shear and growth rate are normalized by the meridional PV jump ϵ. (a) $L/L_R = 0.707$. (b) $L/L_R = 1.697$.

growth rate is shown where more than one unstable mode coexist. There appear two distinct branches in the growth-rate spectra: one that dominates at weak barotropic shear (branch A) and the other that fills the longwave range when shear is large (branch B). As shear increases, the range of wavenumbers over which the branch A is unstable tapers off toward shorter scales and its growth rates decrease substantially. This occurs at much weaker barotropic shear when the meridional separation is larger (Fig. 5b): the branch A exists only for small values of barotropic shear. The growth rates of branch B, on the other hand, become less sensitive to the change in the barotropic shear as it increases, particularly with large L.

To examine more closely the merging of the two branches in the longwave range, especially when the meridional separation is large, a cut along $kL_R = 1$ in Fig. 5b is plotted in Fig. 6, along with the corresponding phase speeds of the modes. The branch A is stationary and has two subbranches. They correspond to the symmetric and antisymmetric modes in the limit of vanishing barotropic shear. It is now clear that the growth rates of the antisymmetric subbranch are masked in Fig. 5 by those of the symmetric subbranch. The branch B emerges when the two subbranches of A coalesce. The two subbranches of B have an identical growth rate and propagate at the same speed but in opposite directions. Similarity to James's (1987) numerical solution (his Fig. 3) is remarkable.

Typical three-dimensional structures of the unstable modes are displayed in Fig. 7 for the two branches. The branch A saddles over the two PV discontinuities (marked by conspicuous peaks in the wave amplitude); that is, it is a meridionally elongated mode. The branch B, in contrast, is highly trapped to near one or the other of the discontinuities. (The upper-layer structure of a subbranch is a mirror image of the lower-layer structure of the other subbranch with opposite phase speed.) That each subbranch of B is influenced by virtually one PV discontinuity implies that it should be approximated by vanishing L (equivalent of a single interface) in (4.2). This roughly explains why the growth rates of the branch B are insensitive to the barotropic shear. In a continuous model such as James's, however, the modal structure undergoes further meridional confinement (his Fig. 4) and reduction in the growth rate (his Fig. 3) as shear increases, a feature that the model with only two PV discontinuities fails to reproduce. (A slight *increase* in growth rates in the *BB'* segment of Fig. 5b levels off as shear increases and should not be taken too seriously.) For both branches, the vertical tilt shown by the upper-layer streamfunction lagging behind the lower-layer phase implies a northward heat flux and is characteristic of baroclinic instability. In addition, a vertically coherent meridional tilt appears in the inner region $-L/2 \leq y$

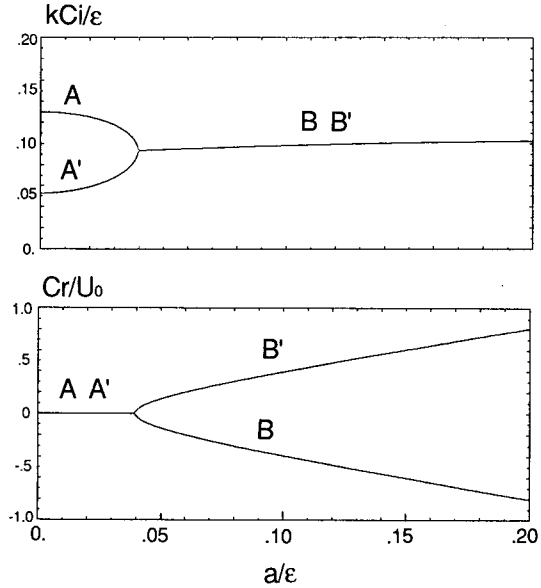

FIG. 6. Growth rate and phase speed of baroclinic waves as a function of basic-state constant barotropic shear. $kL_R = 1$, $L/L_R = 1.697$ (a vertical slice of Fig. 5b). (a) Growth rate (normalized by baroclinic PV jump ϵ) and (b) phase speed (normalized by the thermal wind speed at $y = 0$). Distinct branches and subbranches are labeled.

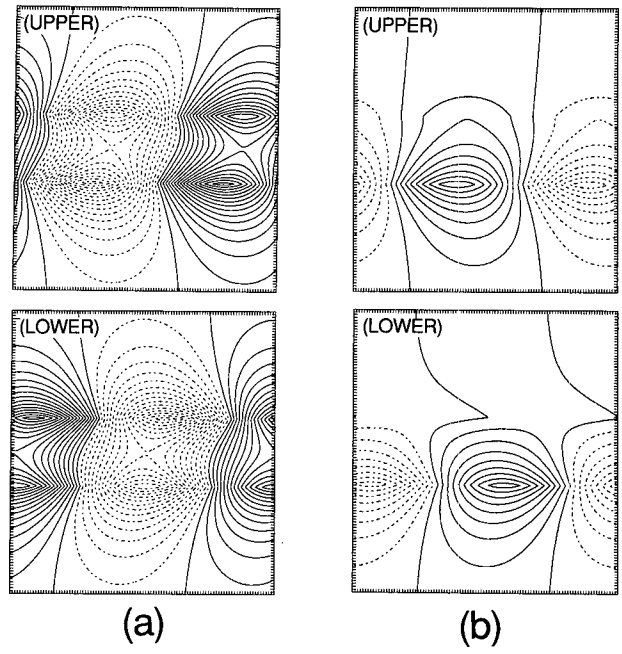

FIG. 7. Three-dimensional structure of streamfunction of the unstable modes. (a) Branch A at $a/\epsilon = 0.02$. (b) Branch B at $a/\epsilon = 0.2$. For both cases $kL_R = 1$ and $L/L_R = 1.697$. Upper panels: horizontal structure of upper-layer streamfunction. Lower panels: horizontal structure of lower-layer streamfunction. Abscissa is x and ordinate is y. The peaks in the amplitudes mark the locations of PV jumps.

$\leq L/2$, particularly with the branch A. The meridional tilt is aligned with the linearly sheared flow, implying that momentum is transported *countergradient.*

Figure 8 is a plot of the vertically integrated momentum flux in the inner region normalized by the kinetic energy of the mode for the corresponding panels of Fig. 5. It is evident that most of the momentum flux is associated with the meridionally elongated mode A, and its direction is predominantly countergradient (indicated by positive values). An explicit parameter dependence of momentum flux is derived for weak shear ($c_i \gg |aL|$) in appendix C, where its countergradient nature is verified for a wide range of k and L.

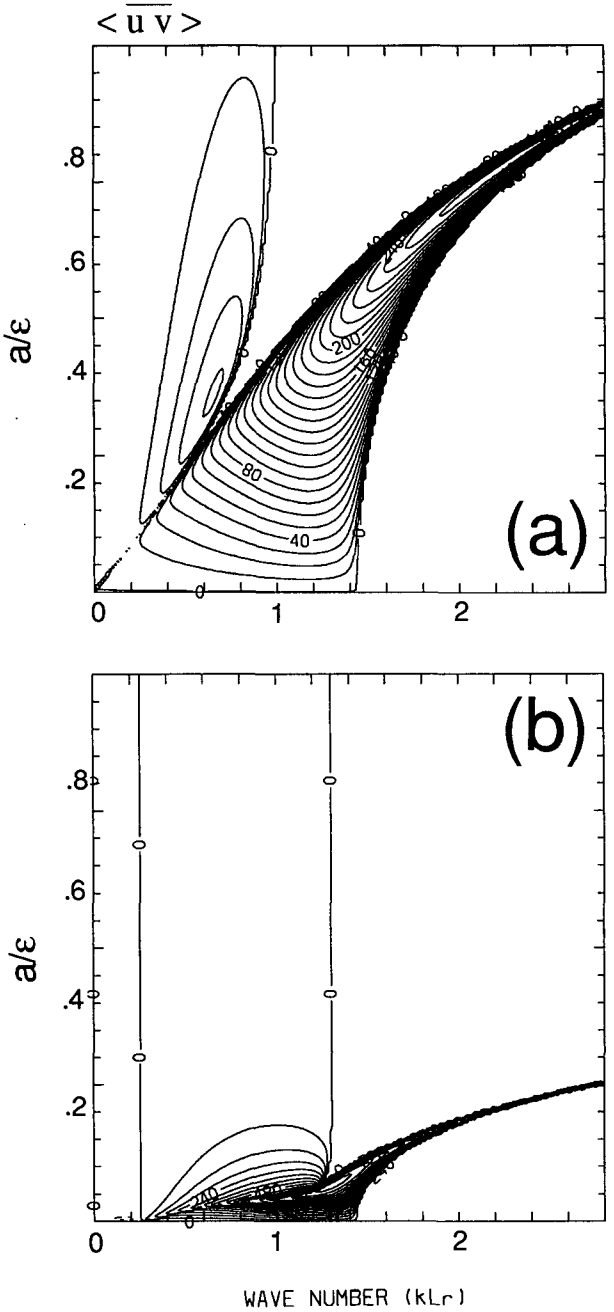

FIG. 8. Same as Fig. 5 but for the vertically integrated momentum flux in the inner region $-L/2 \leq y \leq L/2$. Values are normalized by the eddy kinetic energy. Positive values indicate the countergradient transport of momentum.

Since the momentum fluxes in the outer regions are zero, discontinuities (or delta-function convergence) are formed at $y = \pm L/2$ in the sense to further increase the barotropic shear. This suggests that the normal-mode baroclinic instability developing in a weak barotropic shear would enhance the shear through a positive feedback during its nonlinear life cycle. The spunup shear, in turn, would alter the nature of instability significantly. To see the effects of this self-induced shear, an idealized numerical life-cycle simulation is performed using a multilevel quasigeostrophic model. The model is based on the f plane and Boussinesq approximations. The geostrophically balanced basic flow, illustrated in Fig. 9, is a meridionally symmetric and vertically antisymmetric jet to the lowest order, but is perturbed by a weak, meridionally antisymmetric barotropic flow. Although ideally the simulation should be initialized with the same basic state as in the linear analysis, it is difficult to retain the stepwise discontinuity in the PV against the numerical diffusion in our model. Nevertheless, the smooth profile in Fig. 9 contains essentially the same dynamical ingredients as the discontinuous flow. The most unstable mode is generated using a linearized model and is used to initialize the full model. Throughout the life cycle, a countergradient vertically integrated momentum flux is observed, as well as a downgradient heat flux. As barotropic shear increases due to the momentum transport, the initially coherent meridional structure of the mode breaks up into two trains of eddies at the flanks of the jet, each propagating in the opposite directions, as seen in the evolution of the surface potential temperature (Fig. 9). Transition from a meridionally elongated stationary mode to a pair of counter-propagating modes like the ones found earlier in this section appears to be captured in this more complex numerical model.

It should be added that the vertically integrated momentum flux of a mode is countergradient regardless of the sign of barotropic shear. Thus, whether cyclonic or anticylonic shear emerges during the baroclinic life cycle depends critically on the sign of the barotropic shear initially given. The sensitivity of the finite-amplitude evolution of baroclinic waves to a weak background barotropic shear, demonstrated by Davies et al. (1991) using the semigeostrophic equations, clearly exemplifies this point.

5. Baroclinic instability with linearly sheared jet

While the model introduced in the preceding sections offers a simple tool to examine the coupled barotropic–

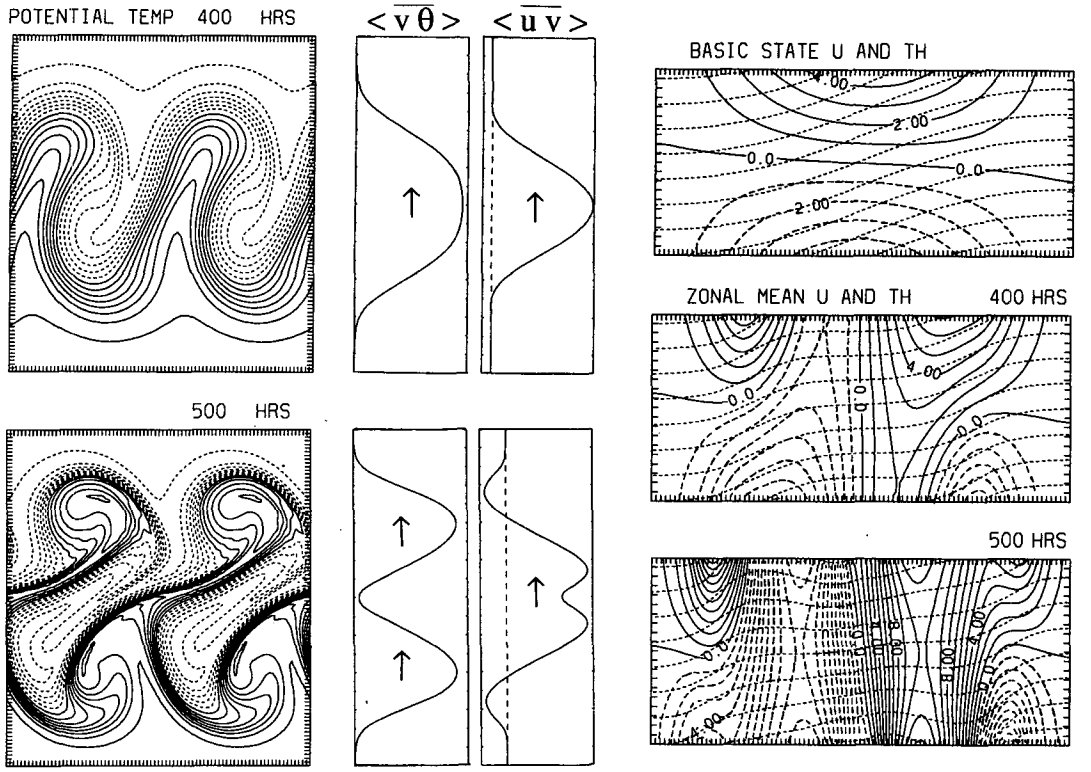

FIG. 9. Time evolution of the surface potential temperature (in x and y) during a life cycle of baroclinic wave with a multilevel QG model (left). The contour interval is 1 K. The meridional profile of the vertically and zonally averaged heat and momentum fluxes (normalized by the maximum values) is shown in the middle. Also shown are the basic-state flow (solid and dashed curves, every 1 m s^{-1}) and potential temperature (thin dashed curves, every 4 K) in y and z, and the modified mean flow at the corresponding time (right). The reentrant channel is 4000 km long (two lengths shown), 10 000 km wide (9000 km shown), and 10 km high. Upper panels: after 400 hours of integration. Lower panels: after 500 hours of integration. The e-folding time for the linear mode is about 100 hours.

baroclinic processes analytically, the analysis is limited to simple flow profiles. A constant, vertically integrated momentum flux can be supported only in the inner region $-L/2 \leqslant y \leqslant L/2$. One cannot simulate, for example, change in the sign of momentum flux within a jet. To allow such variation, one needs more than three meridional regions (thus more than two meridional modes). In principle, one can arbitrarily increase the number of regions to "smooth" the meridional flow profile. This operation also arbitrarily enhances the number of the modes included in the system (as many as the number of PV discontinuities) and thus increases the order of the algebraic equation describing the dispersion relation, quickly invalidating the analytic treatment of the problem. The situation is exactly analogous to increasing the number of layers for better approximation of continuous stratification.

In this section, we add one more region in the meridional direction to examine the stability of a baroclinic flow superposed on a symmetric, linearly sheared barotropic jet. The flow profile we examine is meridionally symmetric about $y = 0$ and given by

$$U_B \equiv \begin{cases} -a(y - L/2), & y \geqslant 0 \\ a(y + L/2), & y < 0 \end{cases} \tag{5.1a}$$

$$U_C \equiv \begin{cases} (\alpha + \beta)\exp\{-(y - L/2)/L_C\}, & L/2 < y \\ \alpha \exp\{-(y - L/2)/L_C\} \\ \quad + \beta \exp\{(y - L/2)/L_C\}, & 0 \leqslant y \leqslant L/2 \\ \alpha \exp\{(y + L/2)/L_C\} \\ \quad + \beta \exp\{-(y + L/2)/L_C\}, \\ & -L/2 \leqslant y \leqslant 0 \\ (\alpha + \beta)\exp\{(y + L/2)/L_C\}, & y < -L/2 \end{cases} \tag{5.1b}$$

$$\alpha \equiv \epsilon L_C\{\exp(-L/2L_C) + 2\}\{\exp(-L/2L_C)\},$$
$$\beta \equiv \epsilon L_C/2, \tag{5.1c}$$

where ϵ is the PV jump associated with U_C at $y = \pm L/2$. A typical flow profile is depicted in Fig. 10. We have now a PV discontinuity at $y = 0$ in addition to at $y = \pm L/2$ in each layer. The shape of U_C is such that the associated PV jump at $y = 0$ is twice that at $y = \pm L/2$. The barotropic flow U_B is a symmetric jet with constant shear on both sides of the axis $y = 0$ and thus by itself does not support instability. Unlike the Couette flow, however, this jet contributes to a PV jump ($=2a$) at $y = 0$, so that the polarity of the PV jumps at the six locations can change depending on the relative magnitude of barotropic and baroclinic components of the flow. As illustrated in Fig. 10, if $\epsilon > a$ the PV jumps change signs vertically at all three interfaces, whereas if $\epsilon < a$ they do not change sign vertically at $y = 0$ but they do meridionally in the lower layer. In terms of the PV dynamics, the latter situation is analogous to a reversed surface potential temperature gradient near the jet axis. The basic flow (5.1) is uniquely determined when ϵ, a, and L are given.

The perturbation streamfunction is sought in the form of (2.7) in each region, subject to the boundary and matching conditions as in section 2 except that we now have an additional interface to match at $y = 0$. A straightforward but tedious algebra leads to six simultaneous linear equations for six independent coefficients

$$\begin{pmatrix} r & S & p & Q & v & W \\ s & R & q & P & w & V \\ 0 & Q & x & Y & 0 & 0 \\ q & 0 & y & X & 0 & 0 \\ 0 & 0 & -x & -Z & x & Z \\ 0 & 0 & -z & -X & z & X \end{pmatrix} \times \begin{pmatrix} A_{\mathrm{II}} \\ B_{\mathrm{II}} \\ C_{\mathrm{II}} \exp(kL/2) \\ D_{\mathrm{II}} \exp(KL/2) \\ A_{\mathrm{III}} \exp(kL/2) \\ B_{\mathrm{III}} \exp(KL/2) \end{pmatrix} = 0, \quad (5.2)$$

where the subscripts II and III denote the two regions $0 \leq y \leq L/2$ and $-L/2 \leq y \leq 0$, respectively, and a dispersion relation

$$(c^4 + M_3c^3 + M_2c^2 + M_1c + M_0)(c^2 - N_0) = 0. \quad (5.3)$$

The expressions for the coefficients in (5.2) and (5.3) are listed in appendix B.

Since we have kept the y symmetry in the basic flow, the symmetric and antisymmetric modes are decoupled in the dispersion relation (5.3). If the symmetry in the basic flow was broken, the sixth-order algebraic equation (5.3) would not be factorized. In the following, we analyze only the symmetric modes represented by the first factor in the lhs of (5.3). Even with this fortuitous factorization, the quartic dispersion relation of the meridionally symmetric modes does not provide much useful information until it is numerically solved, due to the unwieldy forms of the coefficients (appendix B). Figure 11 shows the growth rates normalized by ϵ as a function of nondimensional wavenumber and barotropic shear, plotted for various meridional separations. When the separation is small, unstable modes are found in the longwave range for weak barotropic shear but short waves are also destabilized for strong barotropic shear (Fig. 12a). Large barotropic shear ($a > \epsilon$) makes the configuration of PV jumps like Fig. 10c, and the instability in this range is largely due to the meridional sign change in the PV jumps in the lower layer; that is, it is a close relative of barotropic instability. Yet, this shortwave instability completely disappears at medium to large separation (Fig. 11b,c). In general, the growth rates increase toward zero barotropic shear (baroclinic limit) and toward very large shear (barotropic limit) with a local minimum at an intermediate value. This intermediate value of shear appears to decrease as L increases. The zonal scale of the longwave instability is insensitive to barotropic shear when the meridional separation is large, except that a "tongue" of instability, similar to the one with constant-shear barotropic flow, branches off toward the shorter scales (Fig. 11c).

A cut along $kL_R = 1$ in Fig. 11c is plotted in Fig. 12 with the corresponding phase speeds as a function of barotropic shear. It is clear that what appears connected in the growth rate in Fig. 11c is actually two overlapping but distinct unstable modes. The mode A, with maximum growth rate occurring at zero barotropic shear, is baroclinic instability whose amplitude is maximal at $y = 0$, as shown in Fig. 13a in terms of meridional profile of heat flux. As barotropic shear increases, the growth rate of mode A diminishes while its structure becomes more centralized or decoupled from the PV discontinuities at $y = \pm L/2$ (Fig. 13b). This meridional confinement of the mode is due to the shear effect analogous to the example in the previous section. When the shear a exceeds ϵ, the PV discontinuity at $y = 0$ does not change sign vertically any longer (Fig. 10b,c) and mode A becomes baroclinically stable. The mode B, whose growth rate increases monotonically with barotropic shear (Fig. 12), emerges when the mode A is decoupled from the PV discontinuities at $y = \pm L/2$. The structure of mode B, shown in Fig. 13c, is characterized by maximum heat flux at $y = \pm L/2$, in contrast to the centralized structure of mode A. The mode B is largely sustained by the vertical sign change in PV jumps at $y = \pm L/2$ when the barotropic shear is small, but the meridional sign change in the lower layer becomes equally or more important as barotropic shear increases beyond $a = \epsilon$. The growth rate of mode B exceeds that of A around $a = 0.8\epsilon$. Since the mode A is concentrated near the jet axis, its phase speed exceeds

that of the quasi-stationary mode B. It should be noted that such separation of modes does not occur when the meridional separation is small. For example, a cut at the same wavenumber in Fig. 11b is characterized by a single unstable mode whose growth rate has a minimum near $a = 0.7\epsilon$ but is smoothly connected (not shown). In this case the three PV discontinuities are always bridged by the mode regardless of the magnitude of shear.

Figure 14 is the plot of vertically integrated momentum flux normalized by kinetic energy of the corresponding unstable modes in Fig. 11, measured in the southern half of jet $-L/2 < y < 0$. Due to the symmetry about the jet axis, the momentum flux in the northern half $0 < y < L/2$ is of the same magnitude but the sign is opposite. Therefore, the positive values in Fig. 14 mean a countergradient convergence of momentum (which sharpens the jet), while the negative values indicate a downgradient divergence (which broadens the jet). When the jet is narrow, the momentum flux associated with unstable modes is divergent everywhere, with maximum occurring at short scales with large barotropic shear (Fig. 14a). This is consistent with our previous argument that the shortwave signal is mainly that of barotropic instability. As the meridional separation is increased, the longwave baroclinic instability begins to form a momentum flux convergence at weak barotropic shear, while the momentum flux remains divergent at large barotropic shear (Fig. 14b,c). Similar results have been obtained numerically by Held and Andrews (1983). Notice that there are cuts (discontinuities) in Fig. 14c where the two surfaces, representing the two distinct modes, intersect.

Figure 15 shows the maximum growth rate of the modes, found by scanning across wavenumbers, plotted as a function of separation and meridional shear. The maximum growth rate peaks at vanishing meridional shear and separation, and at large shear and intermediate separation $L \approx L_R$, divided by a "trough" in between. The shaded region is where the most unstable mode produces the momentum flux convergence into the jet. This region exists for a sufficiently large meridional separation ($L > 1.6L_R$) and small shear. The edge of the region, where the vertically integrated momentum flux changes sign, roughly coincides with the trough in the growth rates. It is notable that there is a local minimum in the growth rate around $L = 2.8L_R$ and $a = 0.4\epsilon$.

To see the effects of converging eddy momentum flux in the finite-amplitude evolution of baroclinic instability, we repeat an idealized life-cycle experiment with the same multilevel quasigeostrophic model as used in section 4. This time the basic flow is a meridionally symmetric westerly jet with zero wind at the surface, presumably representing a smoothed version of Fig. 13a. The most unstable mode, generated by the linearized version of the model and used to initialize the simulation, is characterized by a meridionally symmetric structure and by a robust momentum flux convergence into the jet at all levels. As a result, the mean-flow evolution, displayed in Fig. 16, clearly exhibits the acceleration of the jet near the axis and deceleration at the flanks, which strengthens the barotropic shear. As the wave attains finite amplitude, the faster zonal advection near the jet axis than at the flanks distorts its structure, until the meridional coherence is com-

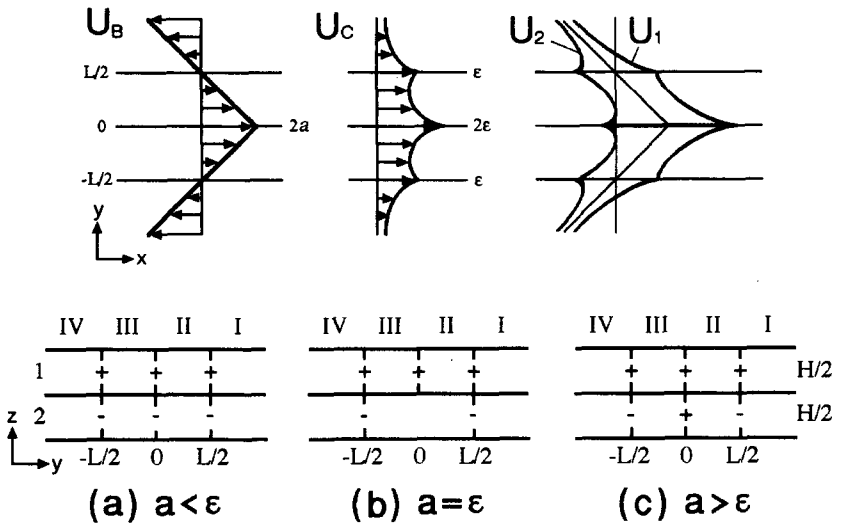

FIG. 10. Geometry of the four-region model with linearly sheared jet. Upper panels illustrate the meridional profiles of barotropic component (left), baroclinic component (center), and upper- and lower-layer flows (right), with the corresponding PV jumps at the kinks labeled. The lower panels: polarity of PV jumps for various magnitude of the point jet. (a) $a < \epsilon$, (b) $a = \epsilon$, and (c) $a > \epsilon$.

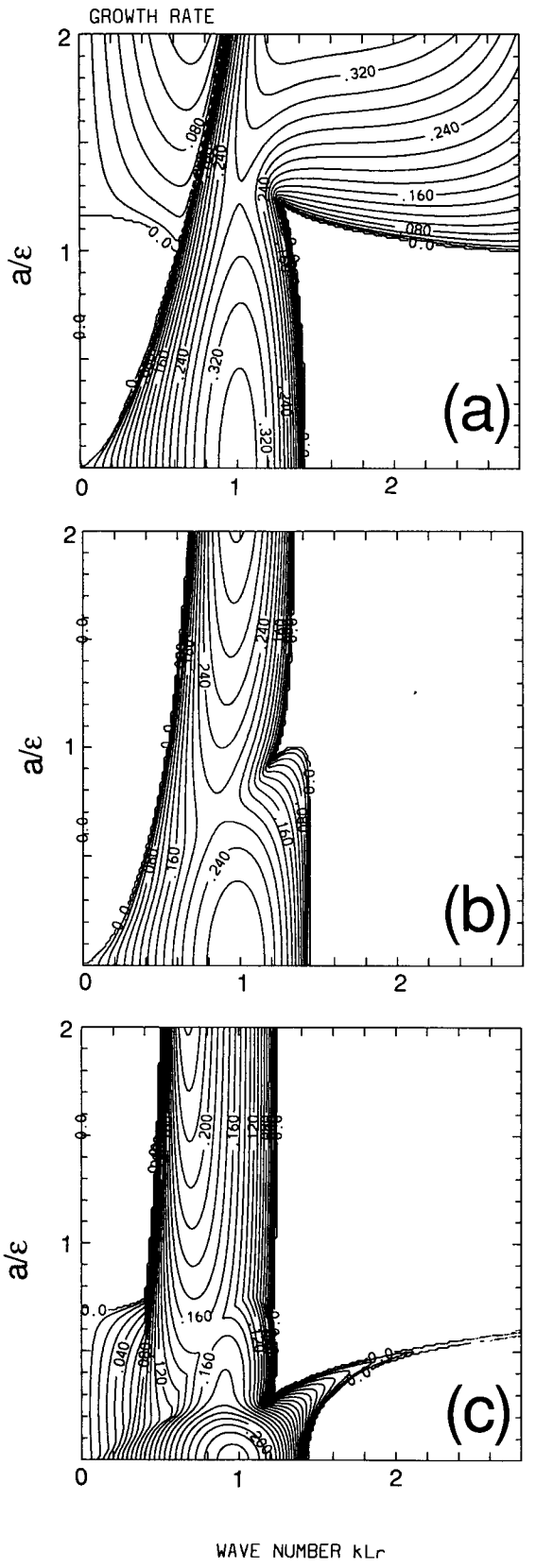

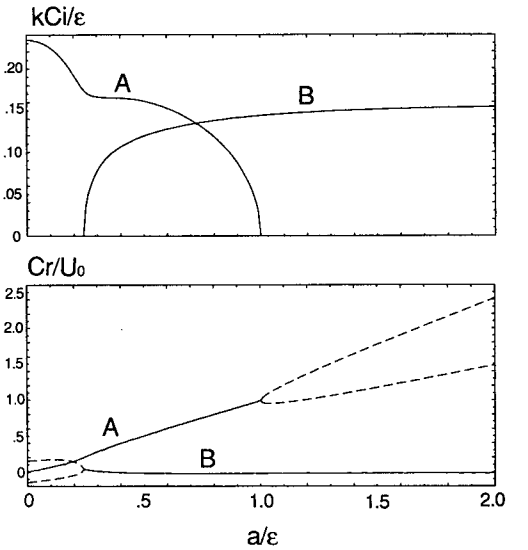

FIG. 12. Growth rate and phase speed of baroclinic waves with linearly sheared jet as a function of barotropic shear. $kL_R = 1$, $L/L_R = 3.111$ (a vertical slice in Fig. 11c). (a) Growth rate (normalized by the PV jump at $y = \pm L/2$). (b) Phase speed (normalized by the thermal wind speed at $y = 0$). Dashed curves in the phase speed represent neutral modes.

pletely destroyed. By this time, the meridional temperature gradient is well mixed (or even reversed) near the jet axis and the strong gradients shift toward the flanks where the flow becomes destabilized again. Accordingly, the maximum in the vertically averaged heat flux moves from the center toward the flanks of the jet. This shift, along with the enhancement of barotropic shear, qualitatively agrees with the sequence in Figs. 13a–c. The effective width of baroclinic zone (equivalent of L) also expands, as indicated by elongated heat flux profile in Fig. 16b, which further favors the meridional separation of modes.

6. Conclusions

We have developed and analyzed a linear model of quasigeostrophic shear instabilities in meridionally, as well as vertically, sheared flows. The model, based on the piecewise constant PV design in the spirit of Eady (1949), requires no slow variation, unlike asymptotic methods, and is analytically tractable for flows with O(1) variation in both dimensions. Although the discontinuous PV makes it difficult to directly relate the results to more realistic flow profiles, the model suc-

FIG. 11. Growth rate of baroclinic instability with linearly sheared jet as a function of wavenumber and barotropic shear. The wavenumber is normalized by the Rossby radius L_R, whereas the shear and growth rate are normalized by the meridional PV jump ϵ. (a) $L/L_R = 0.846$, (b) $L/L_R = 1.980$, and (c) $L/L_R = 3.111$.

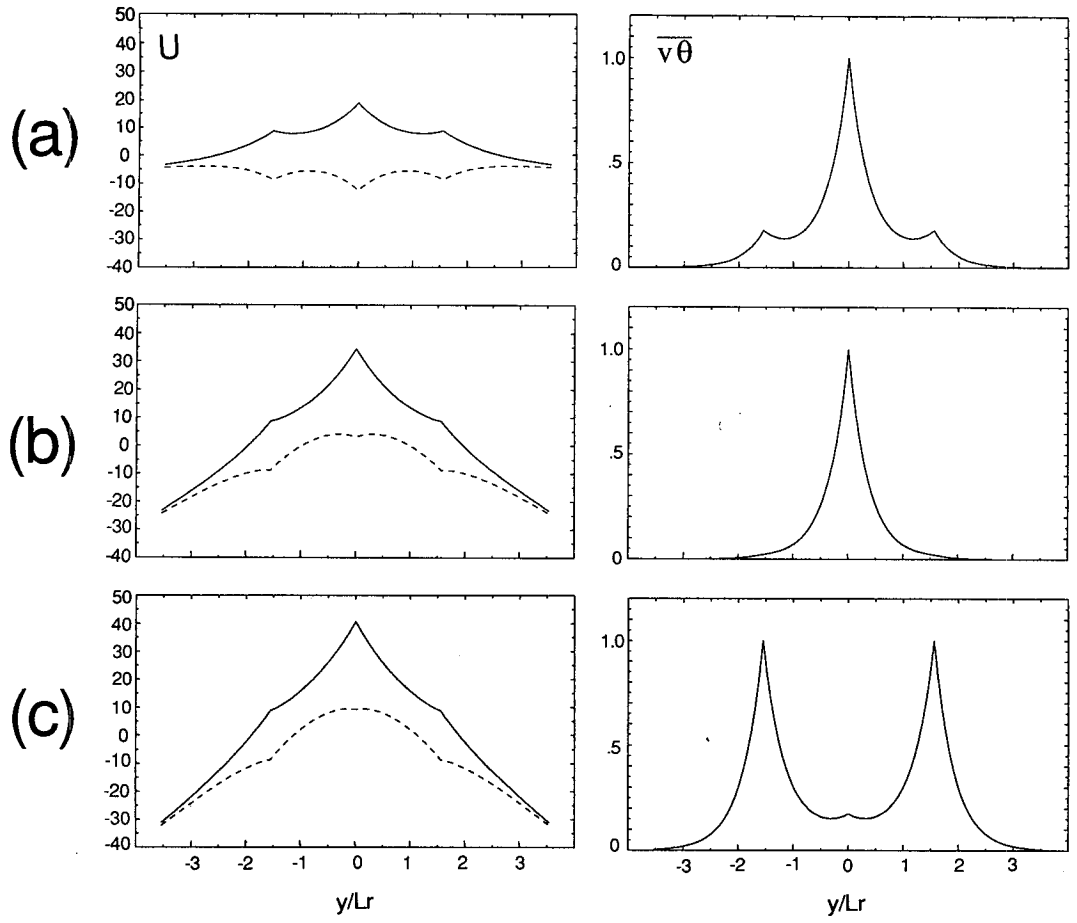

FIG. 13. Meridional profiles of basic flow with linearly sheared jet and heat flux associated with the unstable baroclinic modes. (a) Mode A at $a/\epsilon = 0.1$. (b) Mode A at $a/\epsilon = 0.6$. (c) Mode B at $a/\epsilon = 0.8$. For all cases $kL_R = 1$ and $L/L_R = 3.111$. Solid curve: upper-layer profile. Dashed curve: lower-layer profile. The unit of U is m s^{-1}, assuming $\epsilon = 2 \times 10^{-5}$ s^{-1} and $L_R = 1000$ km. Notice $U_1 - U_2$ is identical in the three plots.

cessfully reproduces qualitative features of more sophisticated numerical calculations. It also enables us to characterize the mode structure and growth rates as functions of a small number of parameters. As a result, exploration of wide parameter range can be achieved inexpensively.

A key aspect in this model is an explicit relationship between the meridional scale of the baroclinic jet and that of modes. The lack of geometrical boundaries or meridional periodicity allows the amplitudes of unstable modes to attenuate away from the meridionally isolated PV discontinuities rather than to have a wavy structure with an arbitrary meridional wavenumber, which is in a sense a more realistic representation of the earth's midlatitude jet. (On the other hand, the model completely lacks the meridional and vertical propagation of Rossby waves.) In the longwave limit, the meridional penetration scale of the mode, L_P, is the zonal wavelength of the mode itself for the barotropic motion (ψ_B) and the internal Rossby radius for the baroclinic motion (ψ_C). The magnitude of L_P relative to the width of the shear zone L (i.e., meridional separation of the PV discontinuities) is an important factor to determine the meridional structure of the mode. The other factors are the magnitude of meridional shear and the PV jumps. Note that the vertical shear is controlled by the PV jumps in the two-layer formulation; thus, it is not an independent parameter like the meridional shear.

The model is capable of predicting simultaneously the heat and momentum fluxes associated with the unstable modes, let alone the growth rates and scales, which is beyond the capability of one-dimensional models. We have demonstrated how the characteristics of baroclinic instability are modified by the background barotropic shear, with an emphasis on the direction of vertically integrated momentum flux. It has been shown that a weak barotropic shear tends to shape baroclinic instability in such a way as to produce a countergradient momentum flux, thereby reinforcing

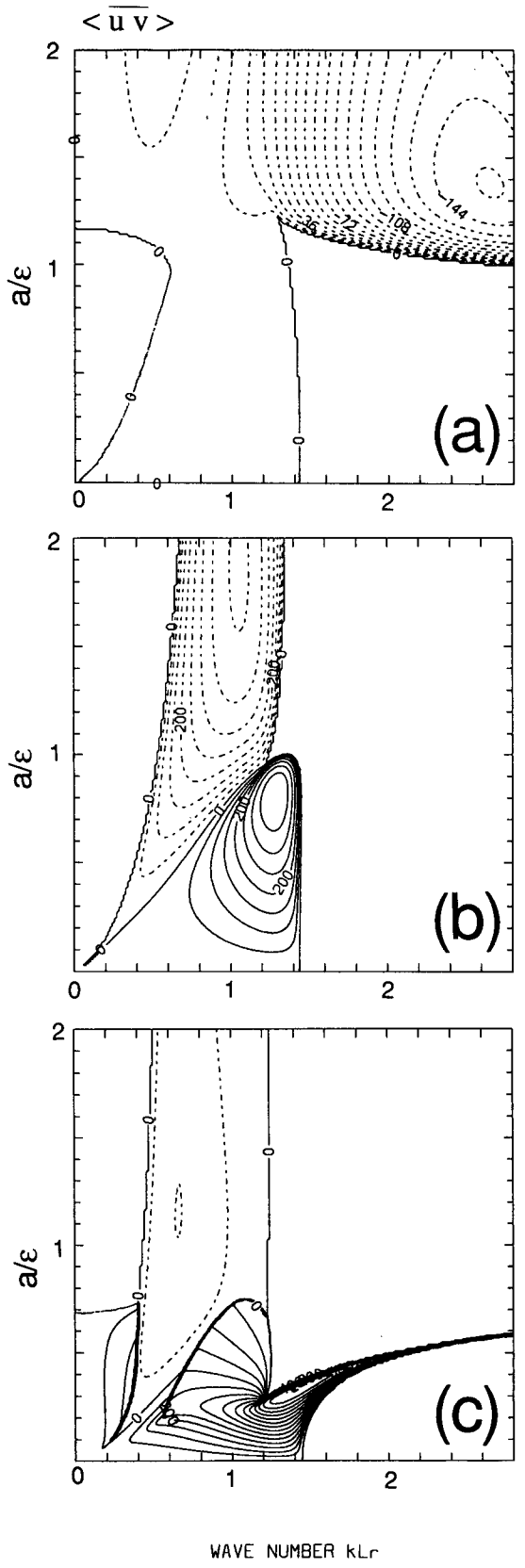

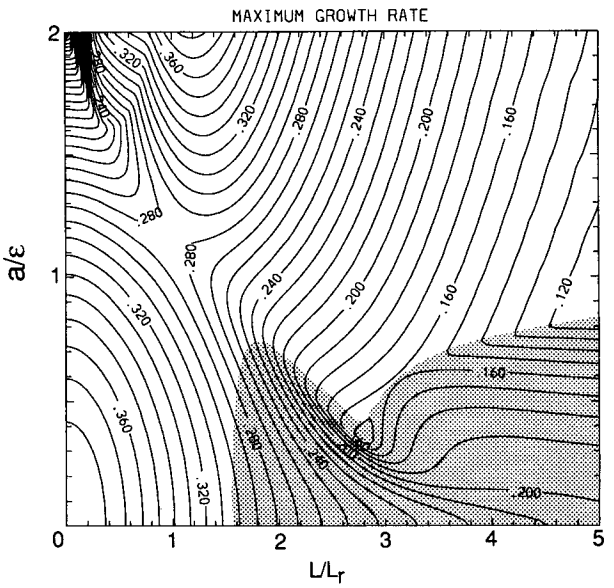

FIG. 15. The maximum growth rates of baroclinic instability with linearly sheared jet, plotted as a function of the meridional separation and the magnitude of the shear. The growth rate is normalized by the baroclinic PV jump ϵ. The stippled region is where the vertically integrated momentum flux associated with the instability is convergent into the jet; elsewhere it is divergent.

the shear. When the shear is too strong, baroclinic instability cannot maintain the meridional coherence and disintegrates into a family of meridionally more confined modes, although the barotropic shear by itself does not eliminate instability. Such transition in the mode structure cannot be captured by any asymptotic methods in which the shear effect is assumed to be small. Our findings are in agreement with previous numerical studies (Stone 1969; Held and Andrews 1983; James 1987).

Finally, this structural change of baroclinic instability due to barotropic shear has been witnessed as a spontaneous process in our idealized numerical life-cycle simulation based on a multilevel model. Because of the positive feedback with the eddy momentum flux, the barotropic shear develops very rapidly and affects the nonlinear life cycle of baroclinic waves. Destruction of potential temperature gradient at the surface still seems necessary to bring the growth of the modes to a halt, but the structure of the equilibrated eddy appears to be very different from what would be predicted by a model excluding the effects of large barotropic shear.

FIG. 14. Same as Fig. 11 but for the vertically integrated momentum flux in the southern half of the jet $-L/2 \leq y \leq 0$. Values are normalized by the eddy kinetic energy. Positive values (solid) indicate convergence of momentum flux into the jet, whereas negative values (dashed) indicate divergence. Thick solid curves in (c) represent the intersection of two distinct modes.

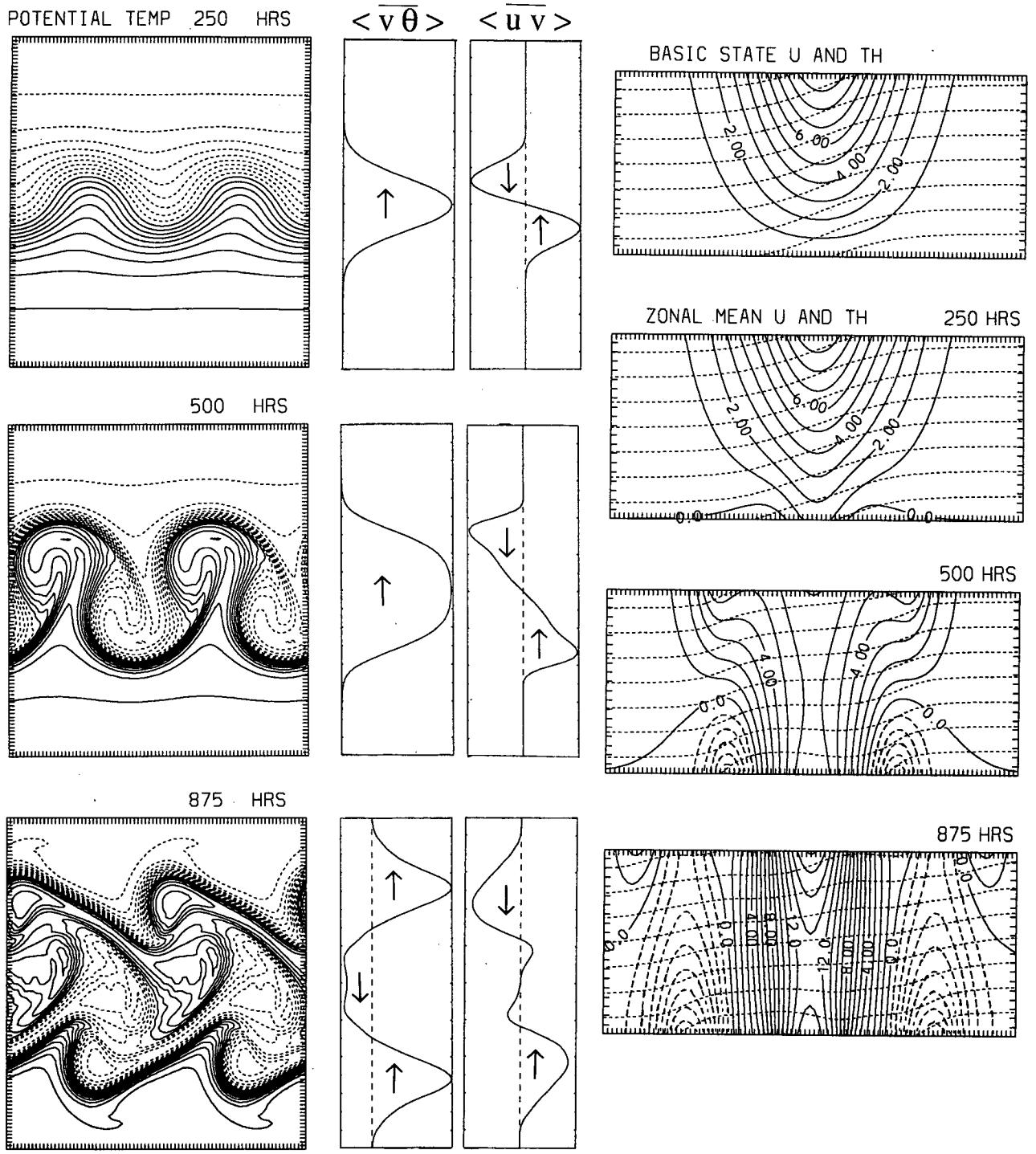

FIG. 16. Same as Fig. 9 but for a vertically asymmetric westerly basic state, shown on the top right. Upper panels: 250 hours after integration, center panels: 500 hours, lower panels: 875 hours. Other parameters are identical with Fig. 10, except that the contour interval for the x–y plot is 0.5 K.

In order to fill the gap between this fully nonlinear, multilevel model and the discontinuous linear model, it is desirable to extend the linear model to a nonlinear regime. The weakly nonlinear theory based on this model, however, does not provide a useful information on the wave–mean flow interaction because of the dis-

continuous nature of the PV profile. It has been shown that the leading nonlinear effect in a model like this is the generation of subharmonics rather than the mean-flow modification (Pedlosky 1985). It is perhaps much simpler to interpret the nonlinear behavior in terms of the displacement of interfaces based on the contour dynamics (Dritschel 1989; Pullin 1992). The rollup of the interfaces at different meridional locations would depend sensitively on their separation and the initial shear.

Acknowledgments. I thank Drs. Isaac Held and Stephen Garner for stimulating discussions, useful comments, and clarification of a number of points in the manuscript. Constructive criticism from Dr. R. T. Pierrehumbert and from an anonymous referee is gratefully acknowledged. The author's research at GFDL has been supported by NOAA Grant NA87EA-D-0A039.

APPENDIX A

Definitions of Coefficients in (3.3) and (3.4)

$$p \equiv 2k$$

$$q \equiv \delta - kaL$$

$$r \equiv \epsilon[1 - kL_C\{1 + \exp(-L/L_C)\}]$$

$$s \equiv \delta \exp(-kL)$$

$$t \equiv \epsilon \exp(-kL)$$

$$w^+ \equiv \frac{q+s}{p} = \delta l^+(k) - aL/2,$$

$$W^+ \equiv \frac{Q+S}{P} = \delta l^+(K) - aL/2,$$

$$z^+ \equiv \frac{r+t}{p} = \epsilon\{l^+(k) - l^+(L_C^{-1})\},$$

$$Z^+ \equiv \frac{R+T}{P} = \epsilon\{l^+(K) - l^+(L_C^{-1})\},$$

$$P \equiv 2K$$

$$Q \equiv \delta - KaL$$

$$R \equiv \epsilon[1 - KL_C\{1 + \exp(-L/L_C)\}]$$

$$S \equiv \delta \exp(-KL)$$

$$T \equiv \epsilon \exp(-KL)$$

$$w^- \equiv \frac{q-s}{p} = \delta l^-(k) - aL/2$$

$$W^- \equiv \frac{Q-S}{P} = \delta l^-(K) - aL/2$$

$$z^- \equiv \frac{r-t}{p} = \epsilon\{l^-(k) - l^+(L_C^{-1})\}$$

$$Z^- \equiv \frac{R-T}{P} = \epsilon\{l^-(K) - l^+(L_C^{-1})\},$$

where

$$l^+(x) \equiv \frac{1 + \exp(-xL)}{2x},$$

$$l^-(x) \equiv \frac{1 - \exp(-xL)}{2x}.$$

APPENDIX B

Definitions of Coefficients in (5.2) and (5.3)

$$p \equiv a \exp(-kL/2),$$

$$r \equiv k(c - bL/2) + b,$$

$$v \equiv -k(c - bL/2)\exp(-kL/2),$$

$$x \equiv 2kc, \quad y \equiv \epsilon - 2k(\alpha + \beta),$$

$$q \equiv \epsilon \exp(-kL/2),$$

$$s = \epsilon - k\{\alpha \exp(L/2L_C) + \beta \exp(-L/2L_C)\},$$

$$w \equiv k\{\alpha \exp(L/2L_C) + \beta \exp(-L/2L_C)\},$$

$$z \equiv \epsilon\{1 - \exp(-kL)\} - 2k(\alpha + \beta)$$

The corresponding parameters in capital letters are obtained by replacing k with K in the above; α and β are defined in (5.1c).

$$M_3 \equiv a\left(\frac{1}{k} + \frac{1}{K} - L\right)$$

$$M_2 \equiv a^2\left(\frac{L}{2} - \frac{1}{k}\right)\left(\frac{L}{2} - \frac{1}{K}\right) - \left(U_0 - \frac{\epsilon}{k}\right)\left(U_0 - \frac{\epsilon}{K}\right) - \{U_L - \epsilon l^-(k)\}\{U_L - \epsilon l^-(K)\} - 2\epsilon^2 \chi(k)\chi(K)$$

$$M_1 \equiv a\left(L - \frac{1}{k} - \frac{1}{K}\right)\{U_L - \epsilon l^-(k)\}\{U_L - \epsilon l^-(K)\} - \epsilon a\{U_L - \epsilon l^-(k)\}\chi^2(K) - \epsilon a\{U_L - \epsilon l^-(K)\}\chi^2(k) - 2\epsilon a(U_0 - \epsilon L/2)\chi(k)\chi(K)$$

$$M_0 \equiv \left\{\left(U_0 - \frac{\epsilon}{k}\right)\left(U_0 - \frac{\epsilon}{K}\right) - a^2\left(\frac{L}{2} - \frac{1}{k}\right)\left(\frac{L}{2} - \frac{1}{K}\right)\right\} \times \{U_L - \epsilon l^-(k)\}\{U_L - \epsilon l^-(K)\} - \epsilon\left(U_0\epsilon - \frac{a^2 L}{2} - \frac{\epsilon^2 - a^2}{K}\right)\{U_L - \epsilon l^-(K)\}\chi^2(k)$$

$$-\epsilon\left(U_0\epsilon - \frac{a^2L}{2} - \frac{\epsilon^2 - a^2}{k}\right)\{U_L - \epsilon l^-(k)\}\chi^2(K) + \epsilon^2(\epsilon^2 - a^2)\chi^2(k)\chi^2(K)$$

$$N_0 \equiv \{U_L - \epsilon l^-(k)\}\{U_L - \epsilon l^-(K)\},$$

where

$$\chi(x) \equiv \frac{\exp(-xL/2)}{x},$$

$$l^-(x) \equiv \frac{1 - \exp(-xL)}{2x}$$

and

$$U_0 \equiv U_C(0) = \alpha \exp(L/2L_C) + \beta \exp(-L/2L_C),$$

$$U_L \equiv U_C(\pm L/2) = \alpha + \beta$$

APPENDIX C

Effects of Barotropic Shear on the Direction of Vertically Integrated Momentum Flux

The parameter dependence of vertically integrated momentum flux (VIMF) is complex. Here we seek an asymptotic expression of VIMF for sufficiently weak barotropic shear, based on the three-region model of section 4. Parameters used in this section are listed in appendix A. When there is no barotropic flow ($a = 0$), the dispersion relation of baroclinic waves reduces to (3.9), where the meridionally symmetric and antisymmetric modes are decoupled. The fastest-growing mode is usually the symmetric mode for which (3.3) can be rewritten

$$\begin{pmatrix} 2kc & 0 & R & T \\ 0 & 2kc & T & R \\ r & t & 2Kc & 0 \\ t & r & 0 & 2Kc \end{pmatrix}\begin{pmatrix} A_0 \\ A_0 \\ B_0 \\ B_0 \end{pmatrix} \equiv \mathbf{P}_0 \cdot \mathbf{a}_0 = 0, \quad \text{(C.1)}$$

where c is a complex root of $\det(\mathbf{P}_0) = 0$, exponentials are absorbed in A_0 and B_0, and

$$c^2 = -c_i^2 = z^+Z^+, \quad z^+ > 0, \quad Z^+ < 0. \quad \text{(C.2)}$$

If we add weak barotropic shear a to the basic flow, (C.1) is modified to

$$(\mathbf{P}_0 + \Delta\mathbf{P} + \Delta\mathbf{Q})\cdot(\mathbf{a}_0 + \Delta\mathbf{a}) = 0, \quad \text{(C.3)}$$

where

$$\Delta\mathbf{P} \equiv \begin{pmatrix} 2k\Delta c & 0 & 0 & 0 \\ 0 & 2k\Delta c & 0 & 0 \\ 0 & 0 & 2K\Delta c & 0 \\ 0 & 0 & 0 & 2K\Delta c \end{pmatrix},$$

$$\Delta\mathbf{Q} \equiv \begin{pmatrix} -kaL & 0 & 0 & 0 \\ 0 & kaL & 0 & 0 \\ 0 & 0 & -KaL & 0 \\ 0 & 0 & 0 & KaL \end{pmatrix}, \quad \text{(C.4)}$$

and $c + \Delta c$ is a root of $\det(\mathbf{P}_0 + \Delta\mathbf{P} + \Delta\mathbf{Q}) = 0$. If the shear is sufficiently small so that

$$|aL|/c_i \equiv \epsilon, \quad \epsilon \ll 1, \quad \text{(C.5)}$$

then $\Delta\mathbf{Q}$ and $\Delta\mathbf{a}$ are merely $O(\epsilon)$ perturbations to $\mathbf{P}_0$ and $\mathbf{a}_0$, respectively. [As it will turn out, $\Delta\mathbf{P}$ is $O(\epsilon^2)$.] Collect through first-order perturbation terms in {(C.3)–(C.1)},

$$\Delta\mathbf{P}\cdot\mathbf{a}_0 + \Delta\mathbf{Q}\cdot\mathbf{a}_0 + \mathbf{P}_0\cdot\Delta\mathbf{a} = 0. \quad \text{(C.6)}$$

Noting the symmetry in the matrices and in the vector $\mathbf{a}_0$, $\Delta\mathbf{a}$ can be split into the symmetric and antisymmetric components:

$$\Delta\mathbf{a} \equiv \Delta\mathbf{a}_s + \Delta\mathbf{a}_a; \quad \Delta\mathbf{a}_s \equiv \begin{pmatrix} \gamma \\ \gamma \\ \delta \\ \delta \end{pmatrix}; \quad \Delta\mathbf{a}_a \equiv \begin{pmatrix} -\alpha \\ \alpha \\ -\beta \\ \beta \end{pmatrix}, \quad \text{(C.7)}$$

thereby, (C.6) is separated to two independent equations for the symmetric and antisymmetric vectors

$$\mathbf{P}_0\cdot\Delta\mathbf{a}_s + \Delta\mathbf{P}\cdot\mathbf{a}_0 = 0,$$

$$\mathbf{P}_0\cdot\Delta\mathbf{a}_a + \Delta\mathbf{Q}\cdot\mathbf{a}_0 = 0, \quad \text{(C.8a,b)}$$

or

$$\begin{pmatrix} 2kc & R + T \\ r + t & 2Kc \end{pmatrix}\begin{pmatrix} \gamma \\ \delta \end{pmatrix} = \begin{pmatrix} -2k\Delta cA_0 \\ -2K\Delta cB_0 \end{pmatrix},$$

$$\begin{pmatrix} 2kc & R - T \\ r - t & 2Kc \end{pmatrix}\begin{pmatrix} \alpha \\ \beta \end{pmatrix} = \begin{pmatrix} -kaLA_0 \\ -KaLB_0 \end{pmatrix}. \quad \text{(C.9a,b)}$$

However, since

$$\begin{vmatrix} 2kc & R + T \\ r + t & 2Kc \end{vmatrix} = 4kK(c^2 - z^+Z^+) = 0 \quad [\text{(C.2)}],$$

(C.9a) is indefinite unless $\gamma = \delta = 0$. Thus, in order for the asymptotic expansion to be consistent, it is required that $\Delta\mathbf{a}_s = \Delta c = 0$, which means the correction in the symmetric component of the mode and in the complex phase speed is at most $O(\epsilon^2)$. Hence

$$\Delta\mathbf{a} = \Delta\mathbf{a}_a. \quad \text{(C.10)}$$

From (C.9b),

$$\alpha = \frac{aL}{2(z^-Z^- - z^+Z^+)}\left(cA_0 - \frac{K}{k}Z^-B_0\right),$$

$$\beta = \frac{aL}{2(z^-Z^- - z^+Z^+)}\left(-\frac{k}{K}z^-A_0 + cB_0\right)$$

if $z^-Z^- - z^+Z^+ \neq 0$, and

$$\alpha = \beta = 0 \quad \text{if} \quad z^-Z^- - z^+Z^+ = 0. \quad \text{(C.11)}$$

Substituting

$$\begin{pmatrix} C\exp(kL/2) \\ A\exp(kL/2) \\ D\exp(KL/2) \\ B\exp(KL/2) \end{pmatrix} \equiv \mathbf{a}_0 + \Delta\mathbf{a} = \begin{pmatrix} A_0 - \alpha \\ A_0 + \alpha \\ B_0 - \beta \\ B_0 + \beta \end{pmatrix}$$

in the expression of VIMF (2.14), then using (C.2), (C.11), and

$$A_0 = -\frac{KZ^+}{kc} B_0, \quad \text{(C.12)}$$

which is a direct consequence of (C.1), one obtains

$$\text{VIMF} = \begin{cases} \dfrac{4aL}{z^+} \dfrac{kc_i}{\epsilon} K^2 |B_0|^2 \dfrac{z^-Z^+ - z^+Z^-}{z^-Z^- - z^+Z^+}, \\ \qquad\qquad z^-Z^- - z^+Z^+ \neq 0 \\ 0, \quad z^-Z^- - z^+Z^+ = 0. \end{cases} \quad \text{(C.13)}$$

Since $z^+ > 0$ [(C.2)], $c_i > 0$, and $\epsilon > 0$, the vertically integrated momentum flux associated with the growing baroclinic wave is positively correlated with the weak barotropic shear (thus countergradient), if the last factor in (C.13) is positive. Numerical evaluation of $z^-Z^+ - z^+Z^-$ indicates its positiveness for all positive k and L (analytical proof would be possible, but messy except for limiting cases). On the other hand, $z^-Z^- - z^+Z^+$ is positive as long as the growth rates of symmetric modes are greater than those of antisymmetric modes, which is true except at very small wavenumbers with large separation (Fig. 4). Hence, the last factor in (C.13) is predominantly positive, confirming the countergradient nature of the momentum flux.

REFERENCES

Charney, J. G., and M. E. Stern, 1962: On the stability of internal baroclinic jets in a rotating atmosphere. *J. Atmos. Sci.*, **19,** 159–172.

Davies, H. C., Ch. Schär, and H. Wernli, 1991: The palette of fronts and cyclones within a baroclinic wave development. *J. Atmos. Sci.*, **48,** 1666–1689.

Dritschel, D. G., 1989: Contour dynamics and contour surgery: Numerical algorithms for extended high-resolution modelling of vortex dynamics in two-dimensional, inviscid, incompressible flows. *Comput. Phys. Rep.*, **10,** 79–146.

Eady, E. T., 1949: Long waves and cyclone waves. *Tellus,* **1,** 33–52.

Fjørtoft, R., 1950: Application of integral theorems in deriving criteria of stability for laminar flows and for the baroclinic circular vortex. *Geofys. Publ.*, **17**(6), 1–52.

Garner, S. T., I. M. Held, and N. Nakamura, 1992: Nonlinear equilibration of two-dimensional Eady waves: A new perspective. *J. Atmos. Sci.*, **49,** 1984–1996.

Gill, A. E., 1982: *Atmosphere-Ocean Dynamics.* Academic Press, 662 pp.

Hayashi, Y.-Y., and W. R. Young, 1987: Stable and unstable shear modes on rotating parallel flows in shallow water. *J. Fluid Mech.*, **184,** 477–504.

Held, I. M., 1975: Momentum transport by quasigeostrophic eddies. *J. Atmos. Sci.*, **32,** 1494–1497.

——, and D. G. Andrews, 1983: On the direction of the eddy momentum flux in baroclinic instability. *J. Atmos. Sci.*, **40,** 2221–2231.

Ioannou, P., and R. S. Lindzen, 1986: Baroclinic instability in the presence of barotropic jets. *J. Atmos. Sci.*, **43,** 2999–3014.

James, I. N., 1987: Suppression of baroclinic instability in horizontally sheared flows. *J. Atmos. Sci.*, **44,** 3710–3720.

Kuo, H. L., 1949: Dynamic instability of two-dimensional nondivergent flow in a barotropic atmosphere. *J. Meteor.*, **6,** 105–122.

Lin, S.-J., and R. T. Pierrehumbert, 1988: Does Ekman friction suppress baroclinic instability? *J. Atmos. Sci.*, **45,** 2920–2933.

McIntyre, M. E., 1970: On the nonseparable baroclinic parallel flow instability problem. *J. Fluid Mech.*, **40,** 273–306.

Moore, G. W. K., and W. R. Peltier, 1987: Cyclogenesis in frontal zones. *J. Atmos. Sci.*, **44,** 384–409.

Pedlosky, J., 1964: The stability of currents in the atmosphere and the ocean: Part II. *J. Atmos. Sci.*, **21,** 342–353.

——, 1985: The instability of continuous Heton clouds. *J. Atmos. Sci.*, **42,** 1477–1486.

——, 1987: *Geophysical Fluid Dynamics.* Springer-Verlag, 710 pp.

Phillips, N. A., 1954: Energy transformations and meridional circulations associated with simple baroclinic waves in a two-level, quasigeostrophic model. *Tellus,* **6,** 273–286.

Pullin, D. I., 1992: Contour dynamics methods. *Ann. Rev. Fluid Mech.*, **24,** 89–115.

Rayleigh, Lord, 1880: On the stability, or instability, of certain fluid motions. *Proc. London Math. Soc.*, **10,** 57–70.

Sakai, S., 1989: Rossby–Kelvin instability: A new type of ageostrophic instability caused by a resonance between Rossby waves and gravity waves. *J. Fluid. Mech.*, **202,** 149–176.

Stone, P. H., 1969: The meridional structure of baroclinic waves. *J. Atmos. Sci.*, **26,** 376–389.